

Exact diagonalization study of the anisotropic Heisenberg model related to YbMgGaO_4 and NaYbCh_2

Muwei Wu, Dao-Xin Yao,^{*} and Han-Qing Wu[†]

State Key Laboratory of Optoelectronic Materials and Technologies,
School of Physics, Sun Yat-Sen University, Guangzhou, 510275, China
(Dated: November 30, 2021)

Employing high-precision exact diagonalization, we systematically study the anisotropic Heisenberg model which is related to rare-earth triangular-lattice materials. From the finite-size low-energy spectra and the finite-size scaling of magnetic orders, we probe the full 3D phase diagram and identify all the phases. Remarkably, we find a large region of quantum spin liquid phase in the model with nearest-neighbor anisotropic exchange interactions. After adding the next-nearest-neighbor interaction, that phase can adiabatically connect to quantum spin liquid phase in the $J_1 - J_2$ triangular Heisenberg model. We also explore the magnetization curves of different phases and reproduce the remnant of 1/3-magnetization plateau in the quantum spin liquid phase. In addition, to study the possible chemical disorders in real materials, we consider the randomness of exchange interactions and find no spin glass order even in the strongest bond randomness case. All of our ED calculations give detailed insightful understanding of the microscopic Hamiltonian related to the YbMgGaO_4 , NaYbCh_2 and some other related rare-earth triangular-lattice materials.

PACS numbers: 71.27.+a, 02.70.-c, 73.43.Nq, 75.10.Jm, 75.10.Kt, 75.10.Nr

Introduction Quantum spin liquid (QSL) phase [1–8] is an exotic quantum phase of matter beyond the Landau-Ginzburg-Wilson symmetry-breaking paradigm and displays rich physics, like nonlocal fractional excitations, long-range entanglement, emergent gauge field. QSLs are more likely to be found in frustrated spin systems, such as triangular and Kagome lattices. The geometric frustration and quantum fluctuation may prevent any magnetic long-range ordering even at zero temperature.

In recent years, two-dimensional rare-earth-based frustrated magnets play an important role and gain much efforts to realize the QSLs. Among that, YbMgGaO_4 [9–14] and rare-earth chalcogenide family NaYbCh_2 (Ch = O, S, Se) [15], are perfect triangular layer compounds with no structural or magnetic transition down to very low temperature. Especially, the broad continuum of magnetic excitation in the inelastic neutron scattering reveals a possible $U(1)$ QSL with a spinon Fermi surface [13, 16]. Unprecedentedly, the magnetic excitation in the fully polarized state at sufficient high field remains very broad in both energy and wave vector, indicating the possible of disorders caused by the site-mixing of $\text{Mg}^{2+}/\text{Ga}^{3+}$, giving rising to the distributions of the effective spin-1/2 g factors and the magnetic couplings [12]. In fact, one recent experiment has observed some spin-glass-like behaviors both in the YbMgGaO_4 and its sister compound YbZnGaO_4 [17].

To understand macroscopic behaviors of these materials, an easy-plane XXZ Hamiltonian with anisotropic exchange interactions was proposed to describe the effective spin-1/2 interactions [10]. This microscopic Hamiltonian was studied by the Luttinger-Tisza method, the classical Monte Carlo simulation, the self-consistent spin wave theory, exact diagonalization (ED) and density-matrix renormalization group (DMRG) [18–24]. In this paper,

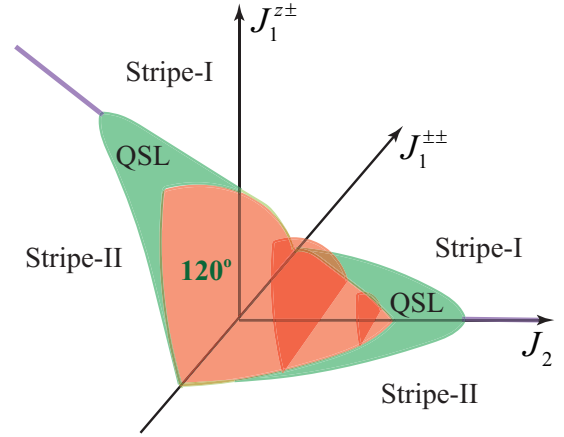


FIG. 1. The sketch of 3D phase diagram of anisotropic triangular Heisenberg model on the $J_2 - J_1^{\pm\pm} - J_1^{\pm\pm}$ parameter space. Four distinct phases, including 120° Néel phase, two stripe phases and the quantum spin liquid phase, are found by our ED calculations. The quantum spin liquid phases of two green-color regions are adiabatically connected without any phase transition.

we use ED to study this anisotropic Heisenberg model related to the YbMgGaO_4 and NaYbCh_2 . We depict the comprehensive 3D phase boundaries using extensive finite-size scaling. We have also studied the magnetic field effects and the bond randomness effects. Many details about the phases have never been revealed before and will provide further insightful understanding of the YbMgGaO_4 and other related materials.

Model and method The generic spin Hamiltonian of YbMgGaO_4 under $R\bar{3}m$ space symmetry group on the

triangular lattice reads,

$$\begin{aligned}
H = & \sum_{\langle i,j \rangle} [J_1 S_i^z S_j^z + \frac{\alpha J_1}{2} (S_i^+ S_j^- + S_i^- S_j^+)] \\
& + J_1^{\pm\pm} (\gamma_{ij} S_i^+ S_j^+ + \gamma_{ij}^* S_i^- S_j^-) \\
& - \frac{i J_1^{\pm\pm}}{2} (\gamma_{ij}^* S_i^+ S_j^z - \gamma_{ij} S_i^- S_j^z + \langle i \leftrightarrow j \rangle) \\
& + \sum_{\langle\langle i,j \rangle\rangle} [J_2 S_i^z S_j^z + \frac{\alpha J_2}{2} (S_i^+ S_j^- + S_i^- S_j^+)] \\
& + \mu_0 \mu_B \sum_i [g_{\perp} (h_x S_i^x + h_y S_i^y) + g_{\parallel} h_z S_i^z]
\end{aligned}$$

It is an easy-plane XXZ Hamiltonian with next-nearest-neighbor and anisotropic off-diagonal nearest-neighbor exchange interactions under external magnetic field. Where $J_1^{\pm\pm}$ and $J_1^{z\pm}$ arise from the strong spin-orbital coupling, $\gamma_{ij} = 1, e^{-i2\pi/3}, e^{i2\pi/3}$ is for the bond along three principle axes, respectively. In the following calculations, we set the XXZ anisotropic $\alpha = 1.317$ [25] and set $J_1 = 1$ for energy unit. In the bond randomness case, The interaction strengths J_{ij} are uniformly distributed in the range $[J_{ij}(1 - \Delta), J_{ij}(1 + \Delta)]$

which are controlled by Δ . $\Delta = 1$ corresponds to the strongest bond randomness case. In the following, we define $H_{\perp} = \mu_0 \mu_B g_{\perp} \sqrt{h_x^2 + h_y^2}$, $H_{\parallel} = \mu_0 \mu_B g_{\parallel} h_z$ as the magnetic-field strengths to simplify the notations.

To get the phase boundaries, we have defined two kinds of magnetic order parameters. The first is the square sublattice magnetization for the 120° Néel phase [24, 26, 27]: $m_N^2 = \frac{1}{3} \sum_{\alpha=1}^3 \left[\frac{1}{(N/6)(N/6+1)} \left\langle \left(\sum_{i \in \alpha} \mathbf{S}_i \right)^2 \right\rangle \right]$, where $\alpha = 1, 2, 3$ represents the three sublattices of the 120° order. The second is the square sublattice magnetization for the stripe phases [24, 27]: $m_{str}^2 = \frac{1}{6} \sum_{v=1}^3 \sum_{\beta_v=1}^2 \left[\frac{1}{(N/4)(N/4+1)} \left\langle \left(\sum_{i \in \beta_v} \mathbf{S}_i \right)^2 \right\rangle \right]$, where $v = 1, 2, 3$ represents three kinds of stripe orders, and $\beta_v = 1, 2$ represents the two sublattices of v -kind stripe order. We use the leading linear scaling $1/\sqrt{N}$ to estimate the magnetic orders in the thermodynamic limit. The finite-size clusters used in the ED calculations are shown in Supplemental Material.

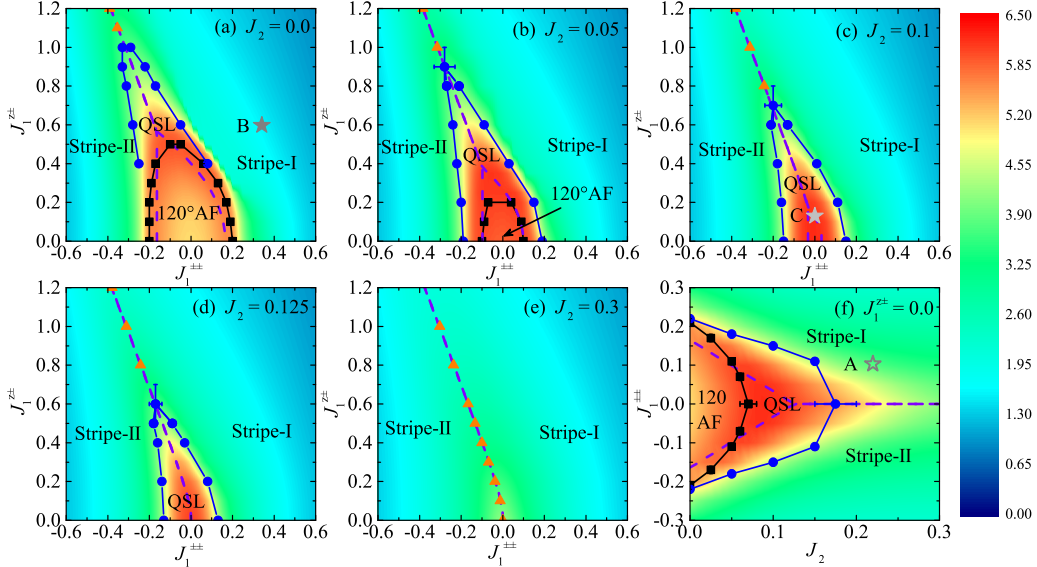


FIG. 2. Phase diagrams on the slices of (a) $J_2 = 0, J_1^{\pm\pm} - J_1^{z\pm}$; (b) $J_2 = 0.05, J_1^{\pm\pm} - J_1^{z\pm}$; (c) $J_2 = 0.1, J_1^{\pm\pm} - J_1^{z\pm}$; (d) $J_2 = 0.125, J_1^{\pm\pm} - J_1^{z\pm}$; (e) $J_2 = 0.3, J_1^{\pm\pm} - J_1^{z\pm}$ and (f) $J_1^{z\pm} = 0, J_2 - J_1^{\pm\pm}$. The color bar shows the strength of frustration parameter f obtained by full exact diagonalization using 12-site cluster (see Supplemental Material). The black and blue phase transition points are obtained from linear extrapolations of finite-size magnetic order parameters, while the yellow points are obtained by the level crossings of low excited energy states (see FIG. 5). The purple dashed lines are the classical phase transition lines between three magnetic phases. The star points A, B and C shown in (f), (a) and (c) denote some sets of exchange parameters fitted by experimental data and get from Ref. 14, Ref. 25 and Ref. 28, respectively. The hollow star point A used a different easy-plane anisotropic $\alpha \approx 1.73$. Some sets of exchange parameters are summarized in Ref. 29.

Phase diagram The sketch of 3D phase diagram was shown in FIG. 1. The red color represents the 120° Néel phase whose region would be shrink after adding the next-nearest-neighbor interaction J_2 . And the green colors on the $J_2 = 0, J_1^{\pm\pm} - J_1^{z\pm}$ and $J_1^{z\pm} = 0, J_2 - J_1^{\pm\pm}$ planes represent the same QSL phase, in the next paragraph, we can show that these two regions can be adia-

batically connected with each other in the $J_2 - J_1^{\pm\pm} - J_1^{z\pm}$ 3D parameter space. We do not observe any multi-Q phase as in the classical Monte Carlo simulation [18]. To see more details of this 3D phase diagram, we plot some slices in FIG. 2. The QSL boundaries are obtained by the vanishing of two kinds of magnetic orders: 120° Néel order and stripe order. Some detailed extrapolations can

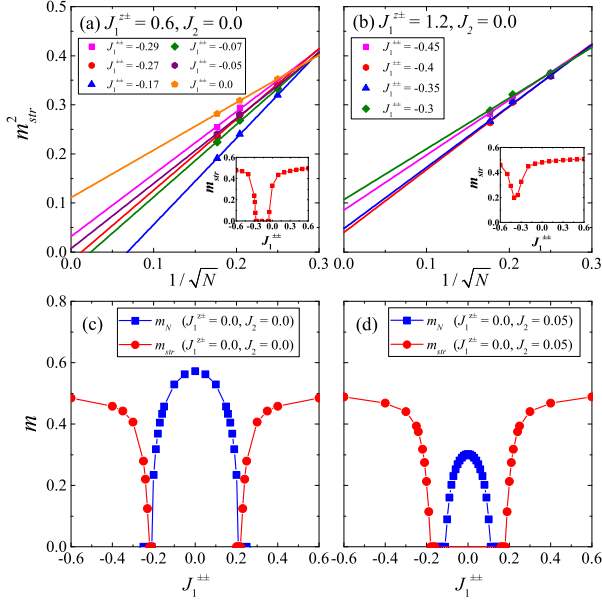


FIG. 3. Linear extrapolations of the square sublattice magnetization for the stripe orders in selective paths which go along (a) $J_1^{z\pm} = 0.6$ and (b) $J_1^{z\pm} = 1.2$ horizontal lines in the phase space of FIG. 2 (a). The extrapolated stripe orders are shown in the insets. When $J_1^{z\pm} = 0.6$, there are two phase transition points at around $J_{1c}^{z\pm} \approx -0.28$ and $J_{1c}^{z\pm} \approx -0.05$. While for $J_1^{z\pm} = 1.2$, the extrapolated stripe order has a minimum at around $J_{1c}^{z\pm} \approx -0.39$ which is a signature of the first-order transition. (c) and (d) are the extrapolated magnetic orders along $J_1^{z\pm} = 0$ horizontal lines in FIG. 2 (a) and FIG. 2 (b), respectively. The 120° Néel phase (blue, square) is sandwiched by two stripe phases (red, circle) at $J_2 = 0$. While at $J_2 = 0.05$, the QSL phase extends to the $J_1^{z\pm} = 0.0$ region.

be seen in Supplemental Material. In FIG. 3, we representatively show the linear extrapolations of magnetic orders along some paths in some 2D slices. In addition, in FIG. 2, we use contour plot to show the frustration parameter $f = |\Theta_{CW}|/T_c$ in the slices, where Θ_{CW} is the negative Curie-Weiss temperature and T_c is the critical temperature. Here, we take the T_c approximately as the temperature where the heat capacity gets its maximum value. We can observe that the QSL region have a larger frustration parameter, especially after adding the next-nearest-neighbor J_2 interaction. The strong frustration in these regions prevent the magnetic ordering even at zero temperature. Under the guidance of the 3D phase diagram, we compare different sets of exchange parameters obtained by different research groups. Most of the parameter sets fall into the stripe phases. We only show three of them which is within or close to the QSL region, labeled with A, B and C in FIG. 2. Here we want to mention that the anisotropic exchange interactions $J_1^{z\pm}$ and $J_1^{\pm\pm}$ are weaker effects from the ESR measurement. However, from our ED calculations, we find that the QSL

region with only nearest-neighbor interactions needs a large $J_1^{z\pm} \sim 0.6J_1$, but it would be reduced by adding the next-nearest-neighbor interaction, which means J_2 is important to capture spin-liquid-behavior of YbMgGaO₄ material if one has to neglect the possible chemical disorders.

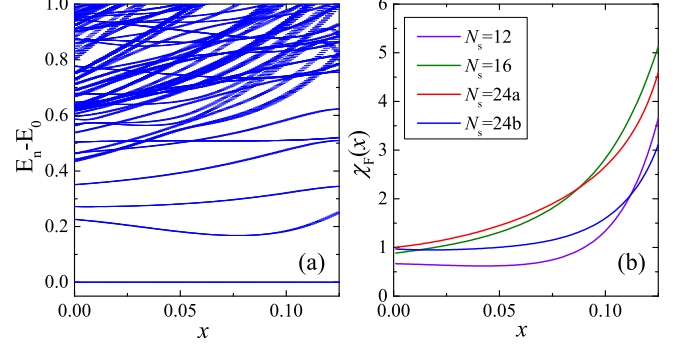


FIG. 4. (a) Low energy spectrum obtained by the 24a cluster and (b) fidelity susceptibility of different clusters change with control parameter x (see the main text for details). The lowest four eigenvalues are in the translation momentum sector of $(k_x = 0, k_y = 0)$. There is no any peak structure among $x \in [0.0, 0.125]$ in the fidelity susceptibility. The increasing behavior near $x = 0.125$ only indicates that it is close to the phase transition point between stripe phase and QSL.

Quantum spin liquid To give a better understanding of the nonmagnetic phases, we have also calculated the chiral and dimer structure factors [24] and got the vanishing extrapolated values. In addition, we have calculated the spin freezing order parameter $\bar{q} = \frac{1}{N} \sqrt{\sum_{ij} [\langle \hat{\mathbf{S}}_i \hat{\mathbf{S}}_j \rangle^2]}$ to detect the possible spin glass order. It also goes to zero within linear extrapolation. Therefore, there is no magnetic orders, chiral order, valence bond solid order and spin glass order in the nonmagnetic region which may be quantum spin liquid phase. Actually, according to the previous numerical and theoretical studies [30–35], a quantum spin liquid phase in $J_1 - J_2$ triangular Heisenberg model is sandwiched between the 120° Néel phase and the stripe phase. In our case with easy-plane anisotropy, the quantum spin liquid region with $J_1^{z\pm} = 0, J_1^{\pm\pm} = 0$ shown in FIG. 2 (f) is about $0.07 < J_2 < 0.175$. After adding the $J_1^{z\pm}$ interaction, this region of quantum spin liquid phase shrinks. To show whether the nonmagnetic phase in the $J_2 = 0, J_1^{z\pm} - J_1^{\pm\pm}$ plane and the quantum spin liquid phase in the $J_1^{z\pm} = 0, J_2 - J_1^{\pm\pm}$ plane is the same phase, we use low energy spectrum and ground state wavefunction to detect the possible gap closing or the sudden change of fidelity susceptibility. The fidelity $F(x) = |\langle \Psi_0(x) | \Psi_0(x + \delta x) \rangle|$ measures the amounts of shared information between two quantum states. If there is a quantum phase transition, a singularity will develop in the fidelity susceptibility defined as $\chi_F(x) = \frac{2[1-F(x)]}{N(\delta x)^2}$. Here, we take

a straight-line path $J_2 = x, J_1^{\pm\pm} = 1.6x - 0.2, J_1^{z\pm} = -5.6x + 0.7, x \in [0, 0.125]$ in the 3D parameter space to show the low energy spectrum and the fidelity susceptibility. From the low energy spectrum of finite-size clusters, no any level crossing or avoided level crossing occurs. From the ground-state fidelity susceptibility shown in FIG. 4, we do not see any discontinuity or divergent tendency as footprints of quantum phase transition. We believe that there would be no quantum phase transition between two nonmagnetic regions in the thermodynamic limit. And they belong to the same quantum spin liquid phase. When $J_2 = 0$, the quantum spin liquid phase is surrounded by two stripe phases and the 120° Néel phase. After adding J_2 , the 120° Néel phase is suppressed, while the area of QSL phase increases first, and then starts to drop, eventually disappears, see FIG. 2 (a-e). In addition, we do not see any quasi-degenerate states of the QSL region in our finite-size calculations. We conjecture that this QSL would be gapless in the thermodynamic limit.

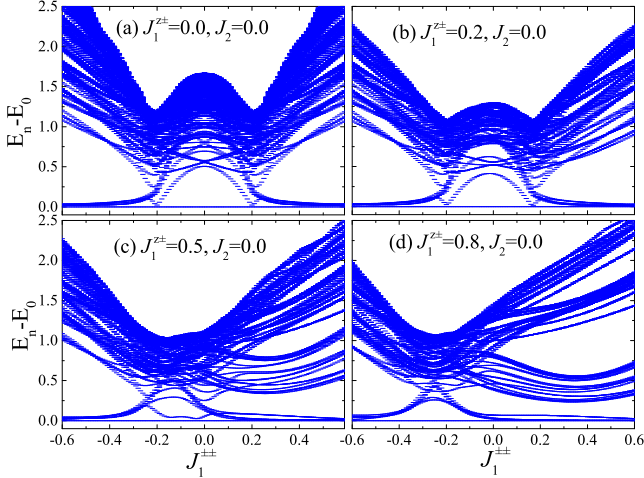


FIG. 5. Low energy spectra of 24a cluster with nearest-neighbor anisotropic interactions. There are six degenerate ground states and a finite excitation gap in the stripe-I and stripe-II phase regions. The inverse “V-shape” in the low energy spectra is more clear when $J_1^{\pm\pm}$ becomes larger. And the tip of inverse “V-shape” can be used to determine the direct (first-order) phase transition points between two stripe phases on different slices [see the yellow triangular point in FIG. 2].

Two stripe phases Next, we want to discuss the stripe-I and stripe-II phases. From the low energy spectra of finite-size clusters shown in FIG. 5, we can conclude that Stripe-I and Stripe-II phases are Ising-like phases that have six degenerate ground states and a finite excitation gap. This degeneracy will be lifted after spontaneously Z_6 discrete symmetry breaking below a finite critical temperature T_c in the thermodynamic limit [22]. More details and discussions about these two stripe phases can be seen in Supplemental Material.

Magnetic field effects Applying magnetic field is a use-

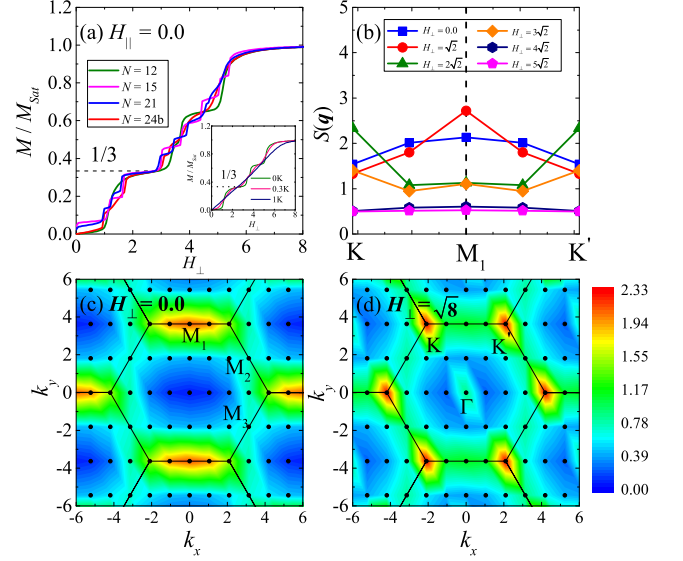


FIG. 6. (a) Magnetization curves of the quantum spin liquid phase at $J_1^{\pm\pm} = -0.17, J_1^{z\pm} = 0.6, J_2 = 0.0$ under external magnetic field applied perpendicular to the c axis. Combined the results of different clusters, a “melting” $1/3$ magnetization plateau is clearly shown near $H_\perp = 2.5$. The inset shows the temperature dependence of magnetization curves obtained by 12-site cluster. (b) The spin structure factors $S(\mathbf{q})$ along $K \rightarrow M_1 \rightarrow K'$ high symmetry path in the Brillouin zone (BZ) under different magnetic fields. With the increasing magnetic field, the spectral weight shifts from M points in the zero field to the K points around the plateau and then transfers to Γ point in the fully polarized phase. (c) and (d) are the contour plots of static spin structure factor in the whole BZ at $H_\perp = 0$ and $\sqrt{8}$, respectively. We use the 24b cluster to get those results in (b), (c) and (d).

ful technique to probe the magnetic system. We have studied the magnetization curves of three magnetic ordered phases and the quantum spin liquid phase. Here in the main text, we only show the magnetization curves at $J_1^{\pm\pm} = -0.17, J_1^{z\pm} = 0.6, J_2 = 0.0$ of QSL region with the magnetic field applied perpendicular to the c axis. Though there are finite-size effects, we still can observe a clear “melting” $1/3$ -magnetization plateau. The nonflatness of this plateau at zero temperature is due to the out of xy plane anisotropic interaction $J_1^{z\pm}$. When the $J_1^{z\pm}$ increases from zero to a large one, the flat $1/3$ -magnetization plateau melts to nonlinear rough curve. Another contribution to the nonflatness of the plateau is the temperature. When the temperature increases, the plateau will further melt to become rough curve. At sufficient high temperature, it becomes a linear curve, which is shown in the inset of FIG. 6 (a). For the spin structure factor $S(\mathbf{q})$, we can observe that the spectral weight shifts from M points in the zero field to the K points in the sufficient strong field around the $1/3$ -magnetization plateau, and then transfers to the Γ point in the fully polarized region. Interestingly, the recent experiment on

the YbMgGaO₄ [28] and NaYbO₂ [36–38] with very low temperature has discovered the non-linearity in the magnetization curve which may be a signature of the remnant of 1/3-magnetization plateau, and it may be seen more clear if further lowering the temperature. The DMRG and classical Monte Carlo simulations using the C set of parameters [see Fig. 2 (c)] have reproduced the non-linearity of magnetization curve. Here, our ED method have reproduced the similar behaviors not only in the C set of parameters but also in large region of QSL phase. What's more, adding J_2 do not change the flatness of the plateau, but the interval of the plateau will shrink. In addition, we have also studied the magnetization curves with the magnetic field parallel to the c axis. The remnant of 1/3-magnetization plateau seems still visible at $J_1^{\pm\pm} = -0.17$, $J_1^{z\pm} = 0.6$, $J_2 = 0.0$, but has a quite narrow interval which is due to the easy-plane anisotropy and the out of plane anisotropic interactions $J_1^{z\pm}$. More details about the magnetization curves of different phases can be seen in Supplemental Material.

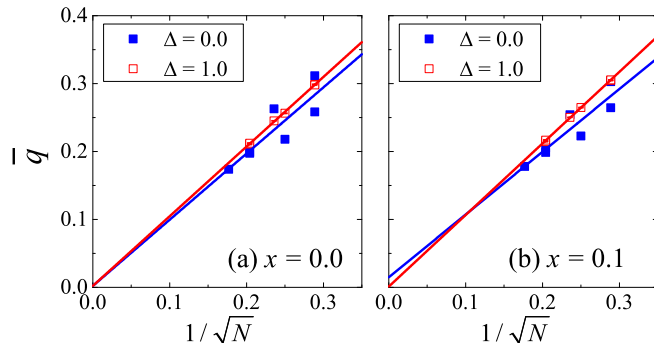


FIG. 7. The spin freezing order parameters \bar{q} in the clean and strongest bond randomness cases. Almost zero extrapolated values indicate there is no spin glass order. We have used at least 50 bond-randomness samples to get the average \bar{q} .

Bond randomness effects To study the possible chemical disorders in real materials, like Ga/Mg mixing in YbMgGaO₄ and Na sites occupied by the Yb ions in NaYbCh₂ [16], we add uniform bond randomness into the Hamiltonian (other distributions of the random exchange couplings do not change the conclusion qualitatively) and discuss the ground state properties. For two stripe phases with finite excitation gaps, the magnetic orders are very stable to the bond randomness and persist up to the strongest randomness $\Delta = 1$. For the 120⁰ Néel order, it is fragile to bond randomness but can persist up to a critical bond randomness strength $\Delta_c < 1$ according to previous ED and DMRG study [24]. So in the strongest bond randomness $\Delta = 1$ case, not only the QSL region but also the stripe phase regions which are very close to the phase boundaries (like A in FIG. 2 (f)) and the whole 120⁰ phase region will show nonmagnetic spin-liquid-like behavior. To detect the possible

spin glass order induced by the bond randomness, we show the spin freezing parameter in FIG. 7. Both in the clean and bond randomness cases, they all are extrapolated to zero. There would be no spin glass order even in the strongest bond randomness case. It may be a 2D random singlet (RS) phase after adding sufficient strong bond randomness in the 120⁰ phase and the QSL phase regions [39]. More discussions about the randomness effects on the stripe-I phase at finite temperature can be seen in Supplemental Material. As for the magnetization curve, the 1/3-magnetization plateau will further melt by the randomness of exchange interactions and g -factors, similar to the temperature effect.

Summary and discussion In summary, we have used ED calculations to get the whole phase diagram in the 3D parameter space. Besides two gapped stripe phases and 120⁰ Néel phase, there is a large nonmagnetic region extending to quantum spin liquid phase in the $J_1 - J_2$ triangular Heisenberg model. Using extensive finite-size scaling, we get the concrete phase boundaries. After applying external magnetic fields, the remnant of 1/3-magnetization plateau can be observed at large region of QSL phase when the magnetic field is perpendicular to the c axis. In addition, we explore the randomness effects. Numerical results show no glass ordering both in the 120⁰ Néel phase and the quantum spin liquid phase. It may be a 2D analog of random-singlet phase in the strongest bond randomness case. Its nature is still a challenge task that leaves for future study.

Acknowledgments H.Q.W. would like to thank Shou-Shu Gong for helpful discussions. The numerical calculations were carried out at the National Supercomputer Center in Guangzhou on the Tianhe-2 platform. D.X.Y. is supported by NKRDPC-2018YFA0306001, NKRDPC-2017YFA0206203, NSFC-11974432, GBABRF-2019A1515011337, and Leading Talent Program of Guangdong Special Projects. H.Q.W. is supported by the National Natural Science Foundation of China through Grant No. 11804401 and the Fundamental Research Funds for the Central Universities.

* yaodaax@mail.sysu.edu.cn

† wuhanq3@mail.sysu.edu.cn

- [1] X. G. Wen, *Phys. Rev. B* **44**, 2664 (1991).
- [2] L. Balents, *Nature* **464**, 199 (2010).
- [3] X.-G. Wen, *Phys. Rev. B* **65**, 165113 (2002).
- [4] A. Kitaev, *Annals of Physics* **321**, 2 (2006).
- [5] L. Savary and L. Balents, *Reports on Progress in Physics* **80**, 016502 (2016).
- [6] M. R. Norman, *Rev. Mod. Phys.* **88**, 041002 (2016).
- [7] Y. Zhou, K. Kanoda, and T.-K. Ng, *Rev. Mod. Phys.* **89**, 025003 (2017).
- [8] C. Broholm, R. J. Cava, S. A. Kivelson, D. G. Nocera, M. R. Norman, and T. Senthil, *Science* **367** (2020), 10.1126/science.aay0668.

- [9] Y. Li, H. Liao, Z. Zhang, S. Li, F. Jin, L. Ling, L. Zhang, Y. Zou, L. Pi, Z. Yang, J. Wang, Z. Wu, and Q. Zhang, *Scientific Reports* **5**, 16419 (2015).
- [10] Y. Li, G. Chen, W. Tong, L. Pi, J. Liu, Z. Yang, X. Wang, and Q. Zhang, *Phys. Rev. Lett.* **115**, 167203 (2015).
- [11] Y. Li, D. Adroja, P. K. Biswas, P. J. Baker, Q. Zhang, J. Liu, A. A. Tsirlin, P. Gegenwart, and Q. Zhang, *Phys. Rev. Lett.* **117**, 097201 (2016).
- [12] Y. Li, D. Adroja, R. I. Bewley, D. Voneshen, A. A. Tsirlin, P. Gegenwart, and Q. Zhang, *Phys. Rev. Lett.* **118**, 107202 (2017).
- [13] Y. Shen, Y.-D. Li, H. Wo, Y. Li, S. Shen, B. Pan, Q. Wang, H. C. Walker, P. Steffens, M. Boehm, Y. Hao, D. L. Quintero-Castro, L. W. Harriger, M. D. Frontzek, L. Hao, S. Meng, Q. Zhang, G. Chen, and J. Zhao, *Nature* **540**, 559 (2016).
- [14] J. A. M. Paddison, M. Daum, Z. Dun, G. Ehlers, Y. Liu, M. B. Stone, H. Zhou, and M. Mourigal, *Nature Physics* **13**, 117 (2016).
- [15] W. Liu, Z. Zhang, J. Ji, Y. Liu, J. Li, X. Wang, H. Lei, G. Chen, and Q. Zhang, *Chinese Physics Letters* **35**, 117501 (2018).
- [16] P.-L. Dai, G. Zhang, Y. Xie, C. Duan, Y. Gao, Z. Zhu, E. Feng, C.-L. Huang, H. Cao, A. Podlesnyak, G. E. Granroth, D. Voneshen, S. Wang, G. Tan, E. Morosan, X. Wang, L. Shu, G. Chen, Y. Guo, X. Lu, and P. Dai, *arXiv* **2004**, 06867 (2020).
- [17] Z. Ma, J. Wang, Z.-Y. Dong, J. Zhang, S. Li, S.-H. Zheng, Y. Yu, W. Wang, L. Che, K. Ran, S. Bao, Z. Cai, P. Čermák, A. Schneidewind, S. Yano, J. S. Gardner, X. Lu, S.-L. Yu, J.-M. Liu, S. Li, J.-X. Li, and J. Wen, *Phys. Rev. Lett.* **120**, 087201 (2018).
- [18] C. Liu, R. Yu, and X. Wang, *Phys. Rev. B* **94**, 174424 (2016).
- [19] Q. Luo, S. Hu, B. Xi, J. Zhao, and X. Wang, *Phys. Rev. B* **95**, 165110 (2017).
- [20] Z. Zhu, P. A. Maksimov, S. R. White, and A. L. Chernyshev, *Phys. Rev. Lett.* **119**, 157201 (2017).
- [21] Z. Zhu, P. A. Maksimov, S. R. White, and A. L. Chernyshev, *Phys. Rev. Lett.* **120**, 207203 (2018).
- [22] E. Parker and L. Balents, *Phys. Rev. B* **97**, 184413 (2018).
- [23] P. A. Maksimov, Z. Zhu, S. R. White, and A. L. Chernyshev, *Phys. Rev. X* **9**, 021017 (2019).
- [24] H.-Q. Wu, S.-S. Gong, and D. N. Sheng, *Phys. Rev. B* **99**, 085141 (2019).
- [25] Y.-D. Li, Y. Shen, Y. Li, J. Zhao, and G. Chen, *Phys. Rev. B* **97**, 125105 (2018).
- [26] K. Watanabe, H. Kawamura, H. Nakano, and T. Sakai, *Journal of the Physical Society of Japan* **83**, 034714 (2014).
- [27] T. Shimokawa, K. Watanabe, and H. Kawamura, *Phys. Rev. B* **92**, 134407 (2015).
- [28] W. M. Steinhardt, Z. Shi, A. Samarakoon, S. Disanayake, D. Graf, Y. Liu, W. Zhu, C. Marjerrison, C. D. Batista, and S. Haravifard, *arXiv* **1902**, 07825 (2019).
- [29] X. Zhang, F. Mahmood, M. Daum, Z. Dun, J. A. M. Paddison, N. J. Laurita, T. Hong, H. Zhou, N. P. Armitage, and M. Mourigal, *Phys. Rev. X* **8**, 031001 (2018).
- [30] R. Kaneko, S. Morita, and M. Imada, *Journal of the Physical Society of Japan* **83**, 093707 (2014).
- [31] P. H. Y. Li, R. F. Bishop, and C. E. Campbell, *Phys. Rev. B* **91**, 014426 (2015).
- [32] Z. Zhu and S. R. White, *Phys. Rev. B* **92**, 041105 (2015).
- [33] W.-J. Hu, S.-S. Gong, W. Zhu, and D. N. Sheng, *Phys. Rev. B* **92**, 140403 (2015).
- [34] Y. Iqbal, W.-J. Hu, R. Thomale, D. Poilblanc, and F. Becca, *Phys. Rev. B* **93**, 144411 (2016).
- [35] S. N. Saadatmand and I. P. McCulloch, *Phys. Rev. B* **94**, 121111 (2016).
- [36] K. M. Ranjith, D. Dmytriieva, S. Khim, J. Sichelschmidt, S. Luther, D. Ehlers, H. Yasuoka, J. Wosnitza, A. A. Tsirlin, H. Kühne, and M. Baenitz, *Phys. Rev. B* **99**, 180401 (2019).
- [37] L. Ding, P. Manuel, S. Bachus, F. Grubler, P. Gegenwart, J. Singleton, R. D. Johnson, H. C. Walker, D. T. Adroja, A. D. Hillier, and A. A. Tsirlin, *Phys. Rev. B* **100**, 144432 (2019).
- [38] J. Guo, X. Zhao, S. Ohira-Kawamura, L. Ling, J. Wang, L. He, K. Nakajima, B. Li, and Z. Zhang, *Phys. Rev. Materials* **4**, 064410 (2020).
- [39] I. Kimchi, A. Nahum, and T. Senthil, *Phys. Rev. X* **8**, 031028 (2018).

Supplemental Material: Exact diagonalization study of the anisotropic Heisenberg model related to YbMgGaO_4 and NaYbCh_2

Muwei Wu, Dao-Xin Yao*, Han-Qing Wu†

*State Key Laboratory of Optoelectronic Materials and Technologies,
School of Physics, Sun Yat-Sen University, Guangzhou, 510275, China*

I. FINITE-SIZE CLUSTERS USED IN THE ED CALCULATIONS

In this paper, we mainly use Lanczos exact diagonalization to get the 3D phase diagram and the low energy spectrum. Meanwhile, we also employ full exact diagonalization to study the finite-temperature properties, such as heat capacity and magnetic susceptibility. To reduce the computational cost, we have used translation symmetry to do block diagonalization. The largest system size in the Lanczos calculations is 32 with the subspace of the largest block up to 0.13 billion.

Seven clusters are mainly used in our ED calculations which are shown in FIG. 8, denoted as 12, 15, 16, 21, 24a, 24b and 32, respectively. The clusters with even number of lattice sites have three M momentum points which are significant for the stripe phases. These three momentum points denote as $M_1 = \frac{1}{2}b_2$, $M_2 = \frac{1}{2}(b_1 + b_2)$, $M_3 = \frac{1}{2}b_1$, where $b_1 = (\frac{2\pi}{a}, -\frac{2\pi}{\sqrt{3}a})$, $b_2 = (0, \frac{4\pi}{\sqrt{3}a})$ are primitive lattice vectors in reciprocal space, a is the lattice constant. Among these five clusters with even number of lattice site, the 12 and 24b clusters also contain two K points, $K_1 = \frac{1}{3}b_1 + \frac{2}{3}b_2$, $K_2 = \frac{2}{3}b_1 + \frac{1}{3}b_2$. The K points are important for 120° Néel phase and the $1/3$ -magnetization plateau phase or “uud” phase. So we use the clusters which contain K points to do the linear extrapolations of 120° Néel order and to get the $1/3$ -magnetization plateau.

Here, we want to mention that three M momentum points are nonequivalent in the 24a, 24b and 32 clusters. Therefore, there may be only one M point which has broad Bragg peak in the spin structure factor $S(\mathbf{q})$ of QSL region (see FIG.6 (c) in the main text). We should see the diffuse magnetic scattering at around all three M points when we use the clusters which have equivalent M points, such as 16 and 6×6 clusters.

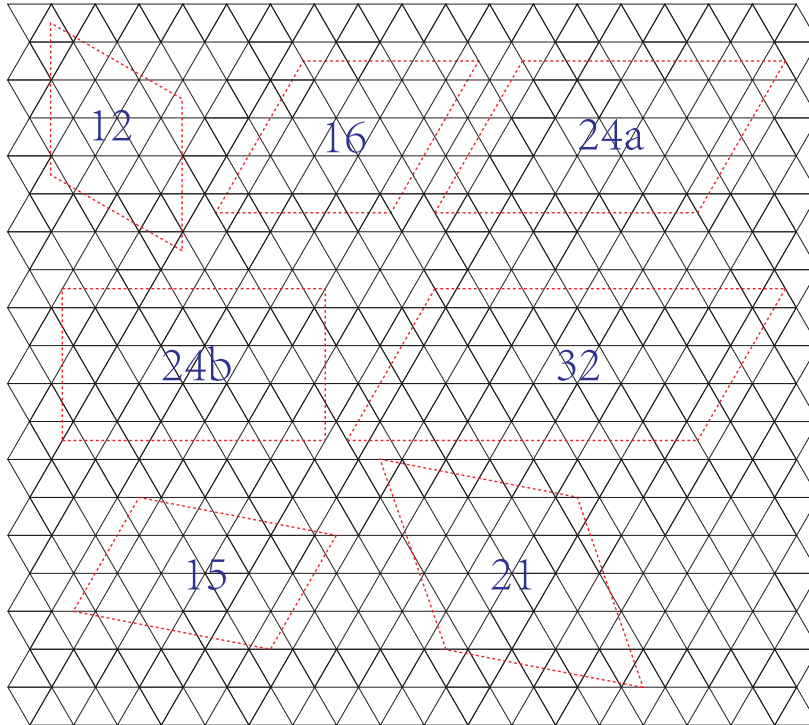


FIG. 8. Finite-size clusters used in the ED calculations. The 12 cluster has been used to do the full exact diagonalization and calculate the frustration parameter.

II: EXTRAPOLATIONS OF MAGNETIC ORDERS

We have representatively shown the linear extrapolations of 120° Néel order and the stripe orders in the main text. Here, we want to show more details about the extrapolations, which are shown in FIG. 9. The magnetic order parameters (square root of the extrapolated results) obtained from FIGs. 9(a1),9(b1),9(a2) and 9(b2) are shown in FIGs. 3(c) and 3(d) in the main text. The largest system size up to 36 sites has been used to do the extrapolations in the easy-plane anisotropic $J_1 - J_2$ Heisenberg model.

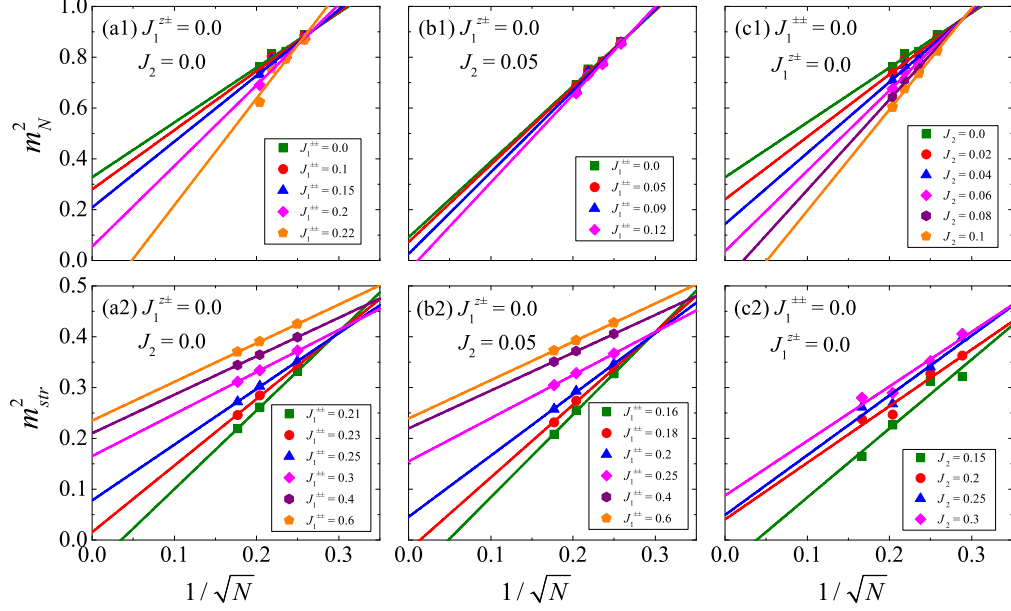


FIG. 9. The linear extrapolations of the square sublattice magnetizations for (a1-c1) the 120° Néel phase and (a2-c2) the stripe phases.

III. STRIPE-I AND STRIPE-II PHASES

In the main text, we have calculated the low energy spectra of different phases and find that there are six degenerate ground states in the stripe phases (see FIG.5 in the main text). These six degenerate ground states are in the translation invariant momentum sectors Γ, M_1, M_2, M_3 . Three of them are in the Γ sector, while the other three distribute into three M sectors. We can use finite-size scaling of energy gaps to verify the degeneracy in the thermodynamic limit which is shown in FIG. 10.

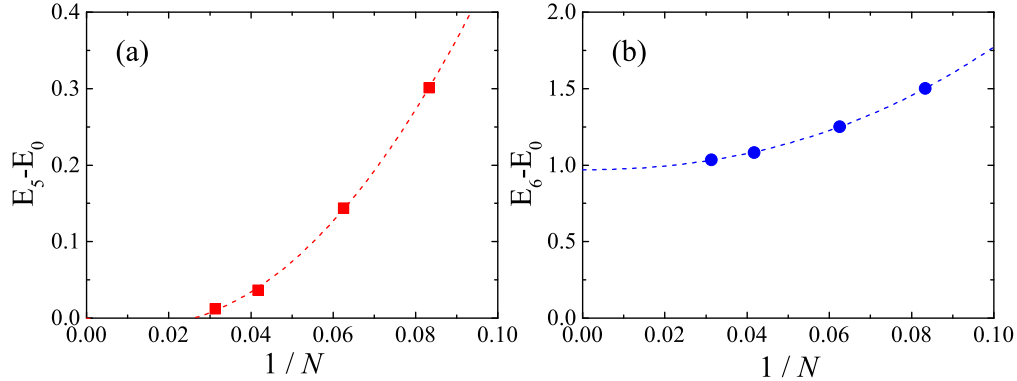


FIG. 10. (a) The third order polynomial extrapolations of (a) the finite-size gap of the six ground state manifolds (GSM) and (b) the excitation gap above the GSM at $J_1^{\pm\pm} = 0.6, J_1^{\pm\pm} = 0, J_2 = 0$ [see FIG. 5(a) in the main text].

Previous study from Ref. 22 has shown that there are six basic spin-orbital-lock stripe configurations which differentiate by three choices of the principal lattice directions that stripes run along and two spin orientations within each stripe. For $J_1^{\pm\pm} = 0$, in the stripe-I phase, the spins lay in the xy plane and point perpendicular to the stripes [see FIG. 11 (a)], while in the stripe-II phase, the spins also lay in the xy plane but point along the principal axes $\pm a_1, \pm a_2, \mp a_1 \pm a_2$ [see FIG. 11 (b)]. The nonzero $J_1^{\pm\pm}$ will tilt the spins out of xy plane by an angle with the z axis.

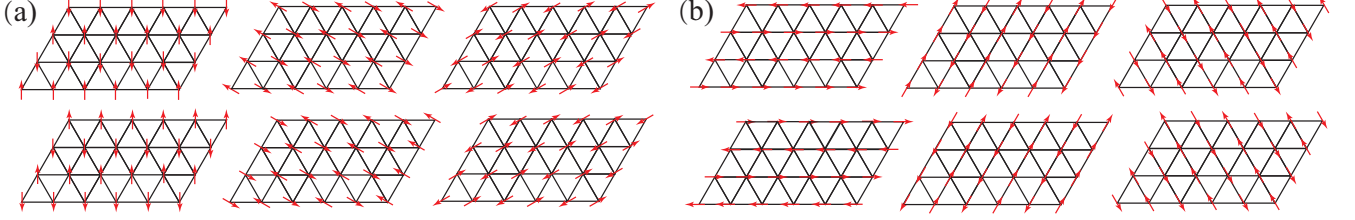


FIG. 11. Six basic magnetic structures for the (a) Stripe-I and (b) stripe-II phases when we take $J_1^{\pm\pm} = 0, J_2 = 0$.

To confirm the magnetic structures in the finite-size ED calculations, we plot the real-space spin correlations of all three components in the limits with only nonzero $J_1^{\pm\pm} = +1$ or $J_1^{\pm\pm} = -1$ or $J_1^{zz} = 1$ which are shown in FIG. 12, FIG. 13 and FIG. 14, respectively. We take the first lattice site as the reference site and show its spin correlations with all other sites. In the $J_1^{\pm\pm} = \pm 1$ case, the spin correlations of the six degenerate ground states in the finite-size ED calculations reflect the superpositions of the corresponding six basic magnetic structures, see FIG. 12 and FIG. 13.

Even though Stripe-I and Stripe-II phases are different phases, we still can use the square sublattice magnetization for the stripe orders (see the definition in the main text) to differentiate them with other phases. And the direction phase transition between two stripe phases will show a dip in the extrapolated results [see the inset of FIG. 3(b) in the main text].

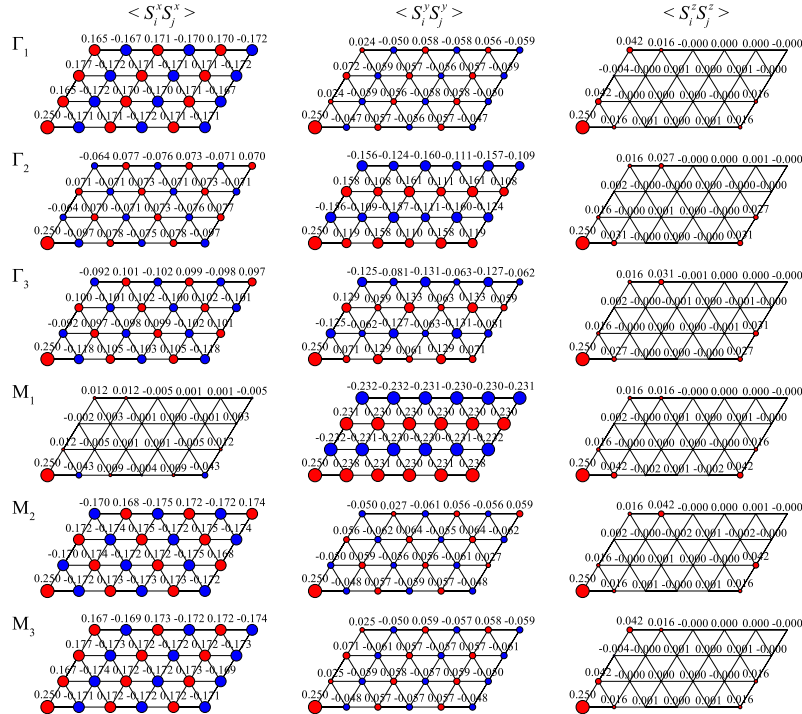


FIG. 12. Three components of the spin correlation functions at the $J_1^{\pm\pm} = +1$ limit with zero values of all other parameters. We use 24a cluster to do the calculations.

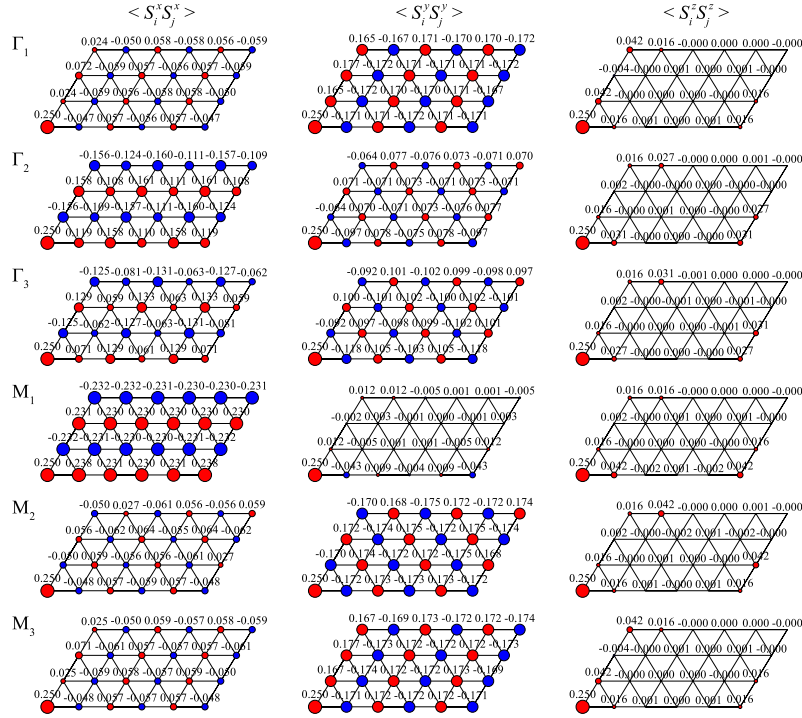


FIG. 13. Three components of the spin correlation functions at the $J_1^{\pm\pm} = -1$ limit with zero values of all other parameters. We use $24a$ cluster to do the calculations.

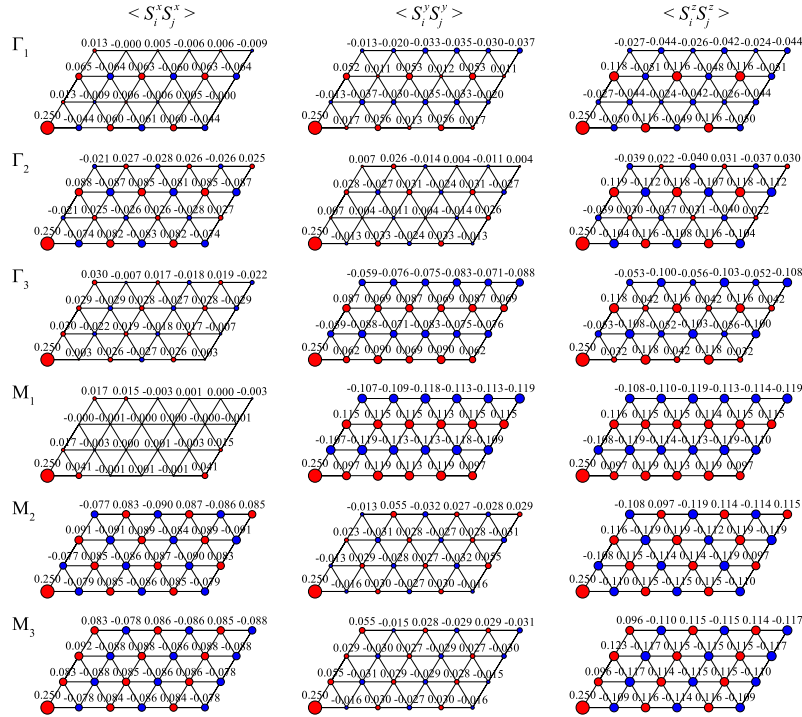


FIG. 14. Three components of the spin correlation functions at the $J_1^{\pm\pm} = 1$ limit with zero values of all other parameters. We use $24a$ cluster to do the calculations.

IV: FRUSTRATION PARAMETER

The frustration parameter is defined as $f = |\Theta_{CW}|/T_c$, where Θ_{CW} is the negative Curie-Weiss temperature and T_c is the critical temperature. We take the T_c approximately as the temperature T_m where the magnetic heat capacity gets its maximum value. Actually, $T_c \approx T_m$ works well in the stripe-I and stripe-II phases. However, in quantum spin liquid phase region, T_c is zero. In fact, the frustration parameter should be diverge. And the heat capacity still has a broad maximum at finite T . In the 120° Néel phase, the $J_1^{\pm\pm}$ and $J_1^{z\pm}$ interactions break the $U(1)$ continuous symmetry of the XXZ model. Especially, the $J_1^{z\pm}$ interaction would tilt the spins out of xy plane. Then whether the 120° Néel phase has a gap and a finite critical temperature are still unclear, which need further study in future. In any case, we can expect that T_c should be lower than the T_m . Therefore, the frustration parameter in the 120° Néel phase is underestimate. Even though, using $T_c \approx T_m$ may not correctly estimate the real frustration parameter. We still can use this approximation to compare the frustration of different phase regions in the 3D parameter space. As we have shown in the FIG.2 of the main text, the nonmagnetic quantum spin liquid region has a larger frustration parameter compared to other magnetic ordered phase regions, that is consistent with phase boundaries obtained by extrapolations of magnetic orders.

Here, we take the B set of parameters [see FIG. 2(a) in the main text] to representatively show the calculation of frustration parameter. The origin data of heat capacity and uniform magnetic susceptibility are shown in FIG. 15. These two observations are calculated by the following equations.

$$C_m = \frac{1}{Nk_B T^2} \left(\langle H^2 \rangle - \langle H \rangle^2 \right), \chi = \frac{1}{Nk_B T} \left(\langle M_z^2 \rangle - \langle M_z \rangle^2 \right)$$

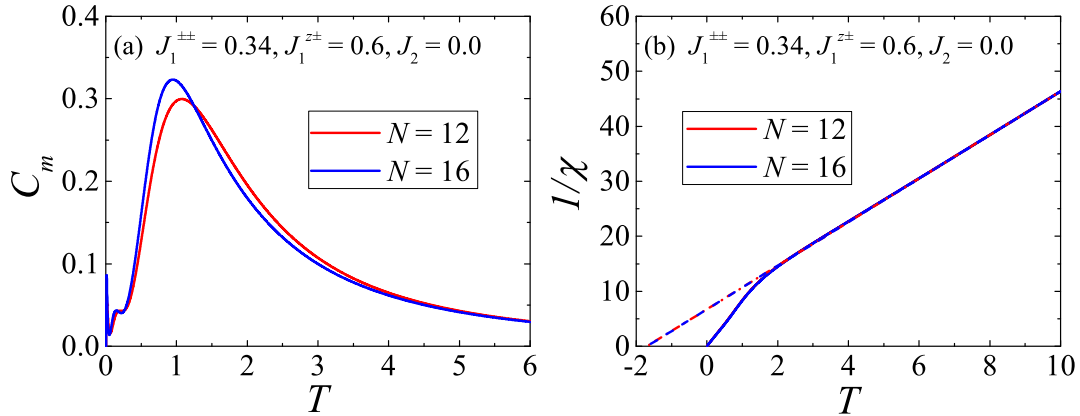


FIG. 15. (a) Magnetic heat capacity and (b) uniform magnetic susceptibility obtained by full exact diagonalization using 12 and 16 clusters. For 12 cluster, $T_m \approx 1.08$, $\Theta_{CW} \approx -1.70$, $f \approx 1.57$. For 16 cluster, $T_m \approx 0.95$, $\Theta_{CW} \approx -1.70$, $f \approx 1.79$. We take the Boltzmann constant $k_B = 1$ in drawing these two figures and use the B set of parameters to do the calculations. Two prominent peaks appear in the heat capacity. The first peak in the low temperature comes from the finite-size gap of ground-state manifold, this peak will shift to zero temperature when the system size goes to infinite. The second peak reflects the finite excitation gap above the GSM, this peak will diverge when the system size goes to infinite which indicates a spontaneously Z_6 symmetry breaking.

V: MAGNETIZATION CURVES

In this sector, we want to show more magnetization curves at different phases, including 120° Néel phase, Stripe-I phase and quantum spin liquid phase. In the main text, we have shown the magnetization curve of the QSL phase at $J_1^{\pm\pm} = -0.17$, $J_1^{z\pm} = 0.6$, $J_2 = 0.0$ under the external magnetic field applied perpendicular to the c axis, a clear $1/3$ -magnetization plateau has been observed. In FIG. 16, we show the magnetization curve of the same set of parameters under the external magnetic field applied parallel to the c axis. The $1/3$ -magnetization plateau seems still visible, but it may be quite narrow in the thermodynamic limit. The different results of two magnetic fields originate from the easy-plane anisotropic $\alpha > 1$ and the out of plane anisotropic $J_1^{z\pm}$.

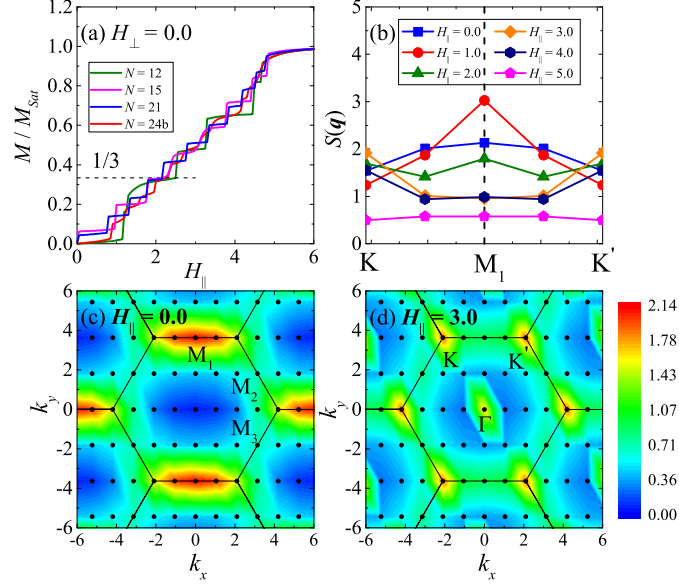


FIG. 16. (a) Magnetization curves of the QSL phase at $J_1^{\pm\pm} = -0.17$, $J_1^{z\pm} = 0.6$, $J_2 = 0.0$ under external magnetic field applied parallel to the c axis. (b) The spin structure factors $S(\mathbf{q})$ along $K \rightarrow M_1 \rightarrow K'$ high symmetry path in the Brillouin zone (BZ) under different strengths of magnetic field. (c) and (d) are the contour plots of spin structure factors in the whole BZ at $H_{\parallel} = 0$ and 3, respectively. We use the 24b cluster to get those results in (b), (c) and (d). The intensity of $S(K)$ at $H_{\parallel} = 3$ is weaker than the intensity of $S(M)$ at $H_{\parallel} = 0$.

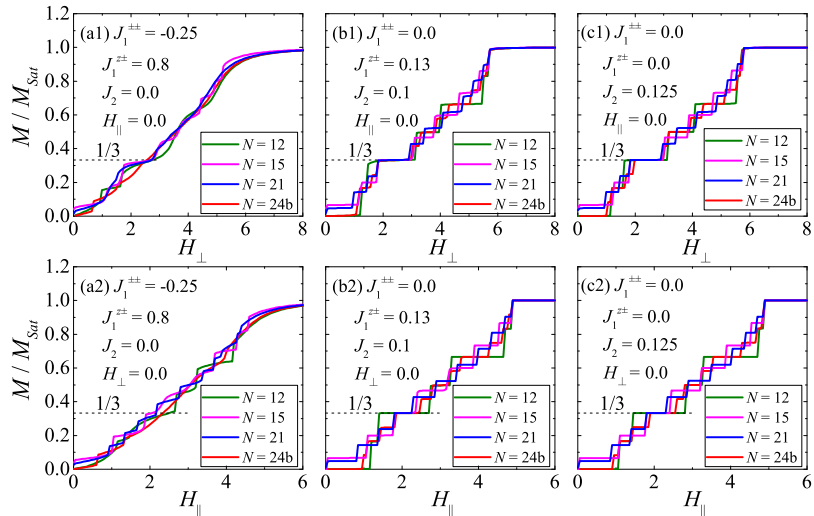


FIG. 17. Magnetization curves of the QSL phase at different sets of parameters under the external magnetic fields. (a1-c1) The magnetic fields are perpendicular to the c axis. (a2-c2) The magnetic fields are parallel to the c axis.

The magnetization curves with other sets of parameters in the quantum spin liquid region are representatively shown in FIG. 17. In FIG. 17 (a), because the out-of-plane interaction $J_1^{\pm\pm} = 0.8$ is large, it seems that the 1/3-magnetization plateau is already melted to be invisible, especially for the curve obtained by 24b cluster. And a more linear curve (in the thermodynamic limit) is observed when applying the field parallel to the c axis. For FIGs. 17 (b1) and 17(c1), the $J_1^{\pm\pm}$ interaction is small or zero, so we can reproduce flat 1/3-magnetization plateaux. The interval of the plateau would be more narrow with the increasing next-nearest-neighbor interaction J_2 .

We have also calculated the magnetization curves of 120° Néel phase and stripe-I phase in FIG. 18. In the 120° Néel phase, the 1/3-magnetization plateau is clearly seen. The nonflatness depends on the $J_1^{\pm\pm}$ interaction. In the stripe-I phase, there is no 1/3-magnetization plateau induced by two kinds of magnetic fields.

To verify the 1/3-magnetization plateau phase is a “uud” phase. We have calculated the energy spectrum and the spin correlation functions at $J_1^{\pm\pm} = -0.17$, $J_1^{\pm\pm} = 0.6$, $J_2 = 0.0$, $H_\perp = 1.8\sqrt{2}$, $H_\parallel = 0$. From the low energy spectrum, we find three-fold (quasi)degenerate ground states. And we show the real-space spin correlation functions of these three ground states in FIG. 19, the “uud” structure can be clearly seen.

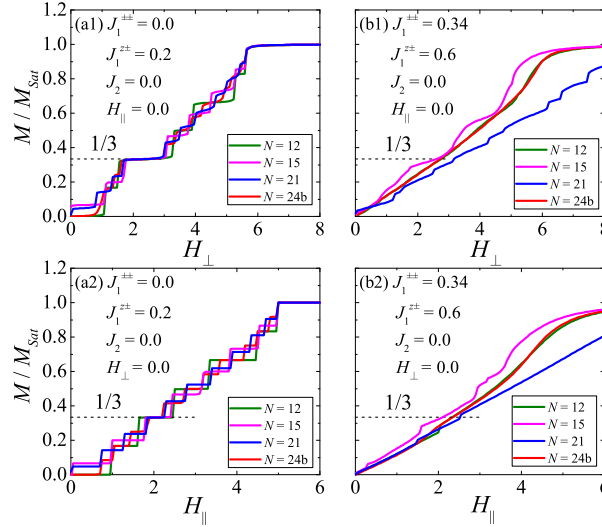


FIG. 18. Magnetization curves at different sets of parameters under external magnetic fields. (a1-b1) The magnetic fields are perpendicular to the c axis. (a2-b2) The magnetic fields are parallel to the c axis. (a1) and (a2) are for the 120° Néel phase. (b1) and (b2) are for the stripe-I phase.

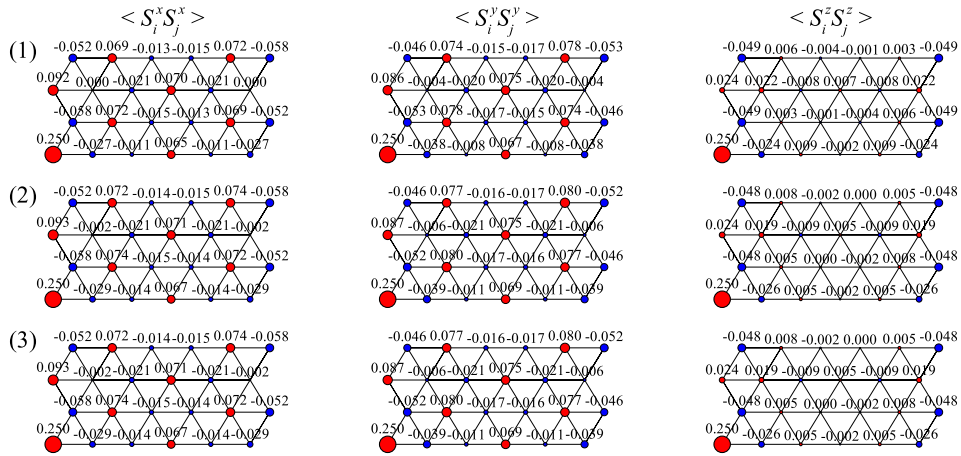


FIG. 19. Three components of the spin correlation functions at $J_1^{\pm\pm} = -0.17$, $J_1^{\pm\pm} = 0.6$, $J_2 = 0.0$, $H_\perp = 1.8\sqrt{2}$, $H_\parallel = 0$.

VI: BOND RANDOMNESS EFFECTS

We have introduced bond randomness into the Hamiltonian to simulate the chemical disorders. For the 120° Néel phase, the strongest randomness at $\Delta = 1$ can eliminate this magnetic order, which can be seen FIG. 20 (a). For the stripe phases, the magnetic orders are stable against the bond randomness. The stripe orders cannot be eliminated even in the strongest bond randomness case, as can be seen FIG. 20 (b).

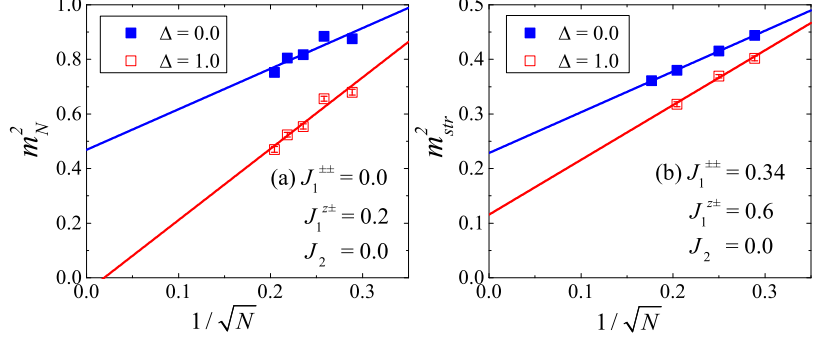


FIG. 20. Linear extrapolations of the square sublattice magnetizations for (a) the 120° Néel phase at $J_1^{\pm\pm} = 0.0$, $J_1^{z\pm} = 0.2$, $J_2 = 0.0$. and (b) the Stripe-I phase at $J_1^{\pm\pm} = 0.34$, $J_1^{z\pm} = 0.6$, $J_2 = 0.0$.

The above discussions focus on ground state properties at zero temperature. Here, we want to discuss the bond randomness effects on stripe-I phase at finite temperature. We take the B set of parameters [see FIG. 2(a) in the main text] to show the measurements. In the strongest-randomness limit, there is only one broad peak in the magnetic heat capacity C_m . Most interestingly, a power-law behavior $C_m \sim T^\delta$ is observed in the low temperature regime, as can be seen in FIG. 21. δ obtained by fitting the C_m curve from $T = 0.1$ K to $T = 0.25$ K using 16 cluster is approximately 0.69 which is very close to $2/3$. And the heat capacity obtained by 12 and 16 clusters under the strongest bond randomness are qualitatively (even quantitatively) the same as the experimental one of YbMgGaO_4 [14, 17]. So surprisingly, a spin-liquid-like behavior has been observed in the strongest bond-randomness limit of the Stripe-I phase.

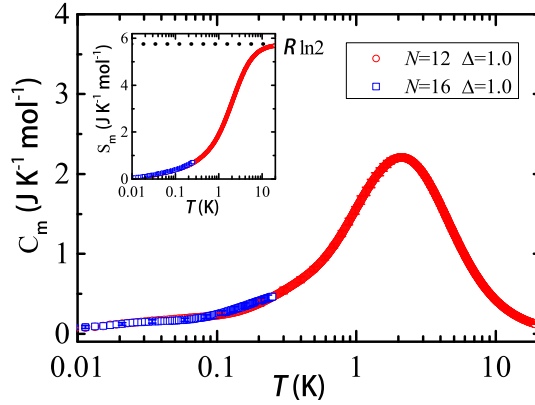


FIG. 21. The magnetic heat capacities C_m obtained by 12 and 16 clusters in the strongest bond randomness limit $\Delta = 1$. Here, we use the B set of parameters: i.e. $J_1^{\pm\pm}/J_1 = 0.34$, $J_1^{z\pm}/J_1 = 0.6$, $J_2/J_1 = 0$, and use $J_1 = 0.164$ meV [25] to do the ED calculations. For the 16 cluster, we employ Lanczos method to calculate the heat capacity at low temperature. The restriction of Boltzmann factor $e^{-(E_{\text{max}} - E_0)/k_B T} < 10^{-12}$ has been used to determine the upper-bound temperature below which the calculated C_m is trustable. And we have used at least 20 bond-randomness samples to get the averaged $C_m(T)$. The inset shows the magnetic entropy $S_m = \int_0^T C_m/T dT$. No residual entropy is found in low temperature.

This may not a coincidence. In the strong randomness case, the finite-size effect is actually not severe. So the 12 cluster is able to capture the main physics in the strongest bond-randomness limit. In this limit, the heat capacity has a broad peak, and this peak will not diverge with the increasing system size. That means even though the ground

state of the system has residual stripe order, but it may be hard to probe this order at finite temperature. Actually, previous classical Monte Carlo simulation from Ref. 22 has shown the similar behavior in the heat capacity. In the clean case, there is a single continuous transition with slowly diverging heat capacity. In the randomness case, this transition is removed by fragmenting the system into domains. This may be one of the possible ways to explain the nonmagnetic behavior down to very low temperature and the glassy behavior shown in *ac* susceptibility (see Ref. 17).